Applied Catalysis B: Environmental 198 (2016) 276–285

Contents lists available at ScienceDirect

Applied Catalysis B: Environmental

journal homepage: www.elsevier.com/locate/apcatb

Construction of novel three dimensionally ordered macroporous carbon nitride for highly efficient photocatalytic activity

Bo Lin[a], Guidong Yang[a,*], Bolun Yang[a], Yuxin Zhao[b,*]

[a] Department of Chemical Engineering, School of Chemical Engineering and Technology, Xi'an Jiaotong University, Xi'an 710049, PR China
[b] State Key Laboratory of Safety and Control for Chemicals, SINOPEC Safety Engineering Institute, Qingdao 266071, PR China

ARTICLE INFO

Article history:
Received 31 March 2016
Received in revised form 26 May 2016
Accepted 28 May 2016
Available online 29 May 2016

Keywords:
Photocatalysis
Three dimensionally ordered macroporous
G-C_3N_4
Structure sensitive property
Active site

ABSTRACT

The construction of multi-porous nanostructured g-C_3N_4 photocatalyst is an efficient strategy to separate charge carriers and enhance the photocatalytic activity in the visible light region. Here we utilized a simply thermal condensation-assisted colloidal crystal template method to construct the novel and highly efficient three dimensionally ordered macroporous (3DOM) g-C_3N_4 photocatalyst for the photocatalytic oxidation of pollutants. The effects of microstructure, crystallinity, textural properties and optical absorption ability on the photocatalytic activity of 3DOM g-C_3N_4 have been systematically probed. Characterization and photocatalytic test results showed that the 3DOM architecture has the unique structure sensitive property to light trapping, reactant transfer and photoreaction, and this property leads 3DOM g-C_3N_4 to produce a narrowed electronic band gap (2.65 eV) and own superior photocatalytic performance for the degradation of organic dye. Compared to pure g-C_3N_4 (lamellar structure), 3DOM g-C_3N_4 shows approximately 5.3 times higher catalytic activity. A possible mechanism of the photoactivity enhancement was proposed based on the photocurrent measurement, photoluminescence analysis and the quenching experiments. This work highlights that the construction of 3DOM architecture could provide a useful strategy to design and fabricate highly efficient g-C_3N_4 photocatalysts.

1. Introduction

The construction of three dimensionally ordered macroporous (3DOM) architecture has been one of the most attractive options to improve the performances and extend the applications of semiconductor materials [1–4]. It has been known that the materials with 3DOM architecture not only possess uniformly distributed macroporous structure and high porosity [5–7], but also own strong photon trapping capacity and electron transport ability [8,9], and these above structure characteristics for the 3DOM semiconductors can be acted as the optical absorption active sites, which can facilitate the light trapping and charge separation and migration. Besides the unique optoelectronic properties, the most attractive feature of the 3DOM materials is their special structure sensitive property for catalytic reaction, because this kind of advanced architecture with an open, interconnected macroporous network could supply a large number of surface defects, step positions and atom vacancies on their inside and outside surfaces, and these unique spots can sever as "interfacial chemical reaction active sites" to enhance the absorption, mass diffusion and removal of reactant during the photocatalytic reaction. Owing to the co-existence of optical absorption active sites and interfacial reaction active sites, the 3DOM materials have shown extremely high use-value in various applications, particular in the solar energy conversion and environmental protection. Till date, various 3DOM photocatalytic materials have been successfully synthesized through the colloidal crystal template method, including 3DOM N-TiO_2 [8], 3DOM $InVO_4$-$BiVO_4$ [9], 3DOM Pr_6O_{11}, 3DOM Tb_4O_7 [10], 3DOM Co_3O_4 [11], etc. All the above-mentioned 3DOM materials show more efficient visible light utilization and improved photocatalytic activity.

Recently, as a new form of metal-free organic semiconductor material, graphitic carbon nitride (g-C_3N_4) has become a hotspot in the field of photocatalysis. This material possesses outstanding optical and electronic properties, remarkable thermal and chemical stability, easily adjustable band structure, low cost and facilely synthetic process [12–14]. However, the traditional two-dimensional lamellar g-C_3N_4 has some prominent disadvantages, such as the relatively narrow visible light responsive region, poor quantum efficiency caused by the high recombination probability of photogenerated electron-hole pairs and the low specific surface area. To overcome the inherent disadvantages of g-C_3N_4, a large num-

* Corresponding authors.
E-mail addresses: guidongyang@mail.xjtu.edu.cn (G. Yang), zhaoyuxin1@yeah.net (Y. Zhao).

http://dx.doi.org/10.1016/j.apcatb.2016.05.069
0926-3373/

ber of strategies have been developed, for instance by doping with nonmetallic elements to harvest a wider portion of solar light [15], by coupling with a narrow matched band gap semiconductor to promote the effective separation of photogenerated charges [16] and by constructing porous nanostructures to increase the photocatalytic reactive surface area [17]. In recent years, preparation of g-C_3N_4 with porous nanostructures, especially with 3DOM structure, has been considered to be a promising way to obtain a high-performance visible-light-induced g-C_3N_4 photocatalyst. As is well known, compared with the two-dimensional lamellar g-C_3N_4, the 3DOM g-C_3N_4 with periodic macroporous structure not only can produce numerous access channels for the mobility of photogenerated carriers and the transfer of reactant species, but also can increase the visible light absorption efficiency induced by multiple scattering and slow photon [3,8]. To date, however, it is still extremely challenging to seek an efficient synthetic approach for 3DOM g-C_3N_4 photocatalyst. Because the common g-C_3N_4 grain with large sheet-like structure is extremely hard to be wrapped and immersed into the interstices of the templates, so that the formation process of three dimensionally ordered macroporous architecture for g-C_3N_4 is quite difficult to achieve under this situation. Until now, to the best of our knowledge, there is few work on studying the 3DOM g-C_3N_4, except the 3DOM g-C_3N_4/C composite very recently reported by Liang et al. [18], which prepared through coupling g-C_3N_4 on the framework of 3DOM carbon material.

In this paper, the novel g-C_3N_4 with three dimensionally ordered macroporous architecture was firstly constructed via a thermal condensation-assisted colloidal crystal template method. It is worth noting that the construction of 3D ordered mesoporous core-shell SiO_2 template is the key step for guaranteeing the successful preparation of 3DOM g-C_3N_4, because this special template can effectively prompt the precursor to fill into the voids in the mesoporous SiO_2 shell and prevent the loss of active ingredients during calcination process. The microstructure, crystal phase, textural properties and optical absorption ability of the obtained photocatalysts were studied by a variety of techniques, and the promising application value of 3DOM g-C_3N_4 was evaluated by the photodegradation of rhodamine B (RhB) under visible-light ($\lambda \geq 420$ nm) illumination. On basis of the characterization and photocatalytic results, the relationship between 3DOM structure and photoactivity of g-C_3N_4 was proposed.

2. Experimental

2.1. Material synthesis

All reagents for synthesis and analysis were commercially available and used without further treatment.

2.1.1. Synthesis of 3D ordered mesoporous core-shell SiO_2 nanospheres

The solid SiO_2 core was prepared according to our previously reported method [19]. Typically, 10 mL of tetraethyl orthosilicate (TEOS) was dispersed in 50 mL of ethanol with vigorous stirring to form solution A, meanwhile, 10 mL of aqueous ammonia and 20 mL of deionized water were added to 50 mL of ethanol with vigorous stirring to form solution B. The solution A and solution B were mixed, constantly stirred and heated at 40 °C for 2.5 h to obtain the uniform SiO_2 nanospheres (solid SiO_2 core). Then a mixture solution of certain amount of TEOS, polyvinylpyrrolidone (PVP) K30 ($M_w \sim 40\,000$) and ethanol was added dropwise to the above silica sol with vigorous stirring at 40 °C for 2 h to form the SiO_2 shell covered on the surface of solid SiO_2 core. And after standing at room temperature overnight, the mixed solution was centrifuged to construct the ordered structure, and then dried at 60 °C in a vacuum drying oven for 12 h. The dried ordered SiO_2 template was calcinated at 700 °C for 6 h in air to remove PVP and obtain the mesoporous shell. The final 3D ordered mesoporous core-shell SiO_2 nanospheres with the average diameter of 280–340 nm were obtained following this way.

2.1.2. Synthesis of 3DOM g-C_3N_4

Certain amount of 3D ordered mesoporous core-shell SiO_2 template was treated with 10 mL of 1 M HCl solution, then dried in a drying oven at 60 °C for 12 h. The treated SiO_2 template was impregnated into 2 g of melted cyanamide liquid at 60 °C for 12 h. Then the mixture was vigorous stirred at 60 °C for 6 h and dried in water bath at 80 °C to obtain white solid. Next, the mixture was calcined at 550 °C for 4 h in a tube furnace with a heating ramp of 2.3 °C min^{-1} in nitrogen atmosphere. Finally, the 3DOM g-C_3N_4 was obtained by removing the 3D ordered mesoporous core-shell SiO_2 template with hydrofluoric acid.

2.1.3. Synthesis of pure g-C_3N_4

2 g cyanamide was directly calcined at 550 °C for 4 h in a tube furnace with a heating ramp of 2.3 °C min^{-1} in nitrogen atmosphere, the resultant canary yellow powder was collected for using as a reference.

2.2. Characterization

The crystal structures of all as-prepared photocatalysts were detected by X-ray diffraction (XRD; SHIMADZU, Lab X XRD-6000). The microstructures and morphologies of all samples were examined by transmission electron microscopy (JEOL, JEM-2100) and scanning electron microscopy (JEOL, JSM-6700F, 200 kV). UV–vis diffuse reflectance spectra (DRS) were recorded on a Hitachi U-4100 UV–vis spectrometer using $BaSO_4$ as the reference. Fourier transform infrared (FT-IR) spectra were conducted on a Nicolet Avatar 360 FT-IR instrument. The textural properties of photocatalysts were investigated using a BET analyzer (ASAP 3000), and specific surface area and pore size distribution of the samples were obtained by the Brunauer-Emmett-Teller (BET) equation and Barrett-Joyner-Halenda (BJH) method, respectively. CO_2 temperature-programmed desorption (CO_2-TPD) tests were performed on a ChemBET Pulsar TPR/TPD apparatus (Quantachrome, U.S.A.) over a temperature range of 60–380 °C at a ramp rate of 10 °C min^{-1} in helium atmosphere. The photoluminescence (PL) emission spectra were measured using a HORIBA JY Fluorolog-3 type fluorescence spectrophotometer with an excitation wavelength of 340 nm.

2.3. Adsorption measurement

The adsorption experiments were executed to investigate the adsorption performances of the samples. Briefly, 0.07 g of the as-prepared photocatalysts were added into 70 mL of Rhodamine B (RhB, 10 mg L^{-1}) aqueous solution and stirred in the dark. Every 5 min, 3 mL of the solution was collected and centrifuged to isolate the photocatalyst powder, and the concentration of filtrated RhB solution was analyzed by a UV–vis spectrophotometer (UV-1900PPC, Shanghai, China) at the maximum characteristic wavelength of 554 nm.

The capacity of the photocatalysts to adsorb RhB molecules can be calculated by the following formula:

$$Q_t = \frac{C_0 - C_t}{M} \times V \quad (1)$$

where Q_t (mg g^{-1}) represents the instantaneous amount of adsorbed RhB on per gram of the photocatalyst (at time t), C_0 and C_t represent the initial and instantaneous (at time t) concentration of

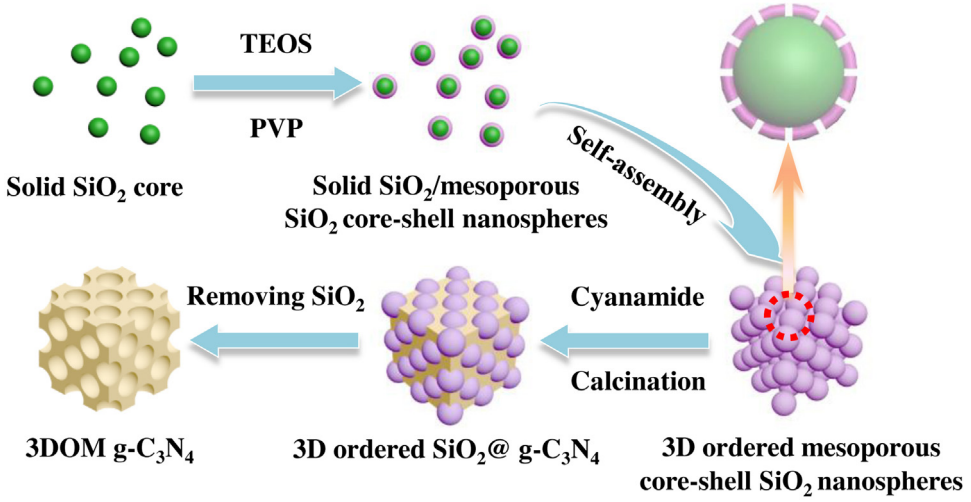

Fig. 1. Schematic illustration of the synthetic strategy of 3DOM g-C_3N_4.

RhB, respectively, *M* represents the mass of the photocatalyst, and *V* represents the volume of the solution.

2.4. Photocatalytic activity measurement

The photocatalytic activities of the samples were evaluated by the degradation of RhB (10 mg L^{-1}) solution with a 300 W Xenon lamp (HSX-F300, Beijing NBeT) as the visible light source ($\lambda \geq 420$ nm). Before illumination, 0.07 g of the photocatalysts were added to 70 mL of RhB aqueous solution and stirred in the dark for 40 min to reach the adsorption/desorption equilibrium. Then the mixed solution was exposed to visible light irradiation ($\lambda \geq 420$ nm) under magnetic stirring. Every 8 min, 3 mL of the solution was withdrawn to isolate the photocatalysts. Similarly to the adsorption experiments, the concentration of residual RhB solution was tested by the above UV–vis spectrophotometer. The recycled experiments were carried out under the same reaction conditions to further investigate the reusability and stability of the 3DOM g-C_3N_4 sample. After every 40 min photoreaction, the separated photocatalyst particles were washed and dried for 4 h at 80 °C, then put into the same volume of fresh RhB solution (10 mg L^{-1}) to perform the next cyclic experiment. To shed light on the main reactive oxygen species, the quenching texts of the active species were performed by using different scavengers.

2.5. Photoelectrochemical measurement

The photocurrent response and electrochemical impedance spectra (EIS) of the as-prepared photocatalysts were assessed on an electrochemical station (CHI 660D, Chenhua, Shanghai, China) in a typical three-electrode system, whose electrolytes were Na_2SO_4 aqueous solution (2 M) and the mixed solution of KCl (0.2 M) and $K_3[Fe(CN)_6]$ (0.005 M) with the volume ratio of 1:1, respectively. A platinum wire and Ag/AgCl (3 M KCl) were served as the counter electrode and the reference electrode, respectively. The glassy carbon electrodes (GCE, 0.07065 cm^2) modified with pure g-C_3N_4 and 3DOM g-C_3N_4 were used as the working electrodes.

3. Results

The overall synthetic strategy of 3DOM g-C_3N_4 is schematically displayed in Fig. 1. The initial SiO_2 nanosphere collosol (solid SiO_2 core) was synthesized based on a modified Stöber's method mentioned in our previous paper [19]. And then another batch of TEOS, EtOH and the desired amount of PVP was added dropwise into SiO_2 nanosphere collosol, where PVP was used as the porogen agent to generate a mesopores SiO_2 shell under solvothermal condition. After that, a layer of mesoporous silica was covered on solid SiO_2 core to form core-shell silica material. In the following step, these monodisperse core-shell SiO_2 nanospheres can be easily self-assembled to obtain 3D ordered opal frame through a centrifugation method. Subsequently, the as-prepared 3D ordered SiO_2 array was calcined at 700 °C in order to completely remove the PVP surfactant and thus generate multitudinous pores in the

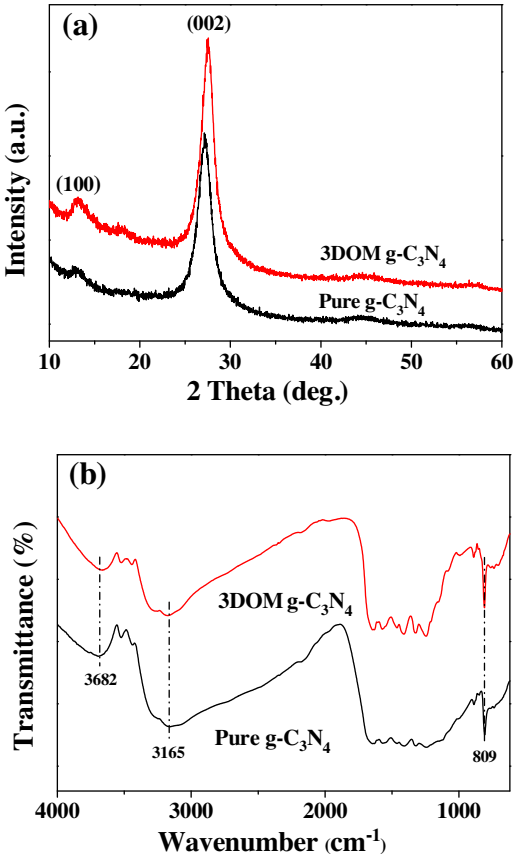

Fig. 2. X-ray diffraction patterns (a) and FT-IR spectra (b) of pure g-C_3N_4 and 3DOM g-C_3N_4.

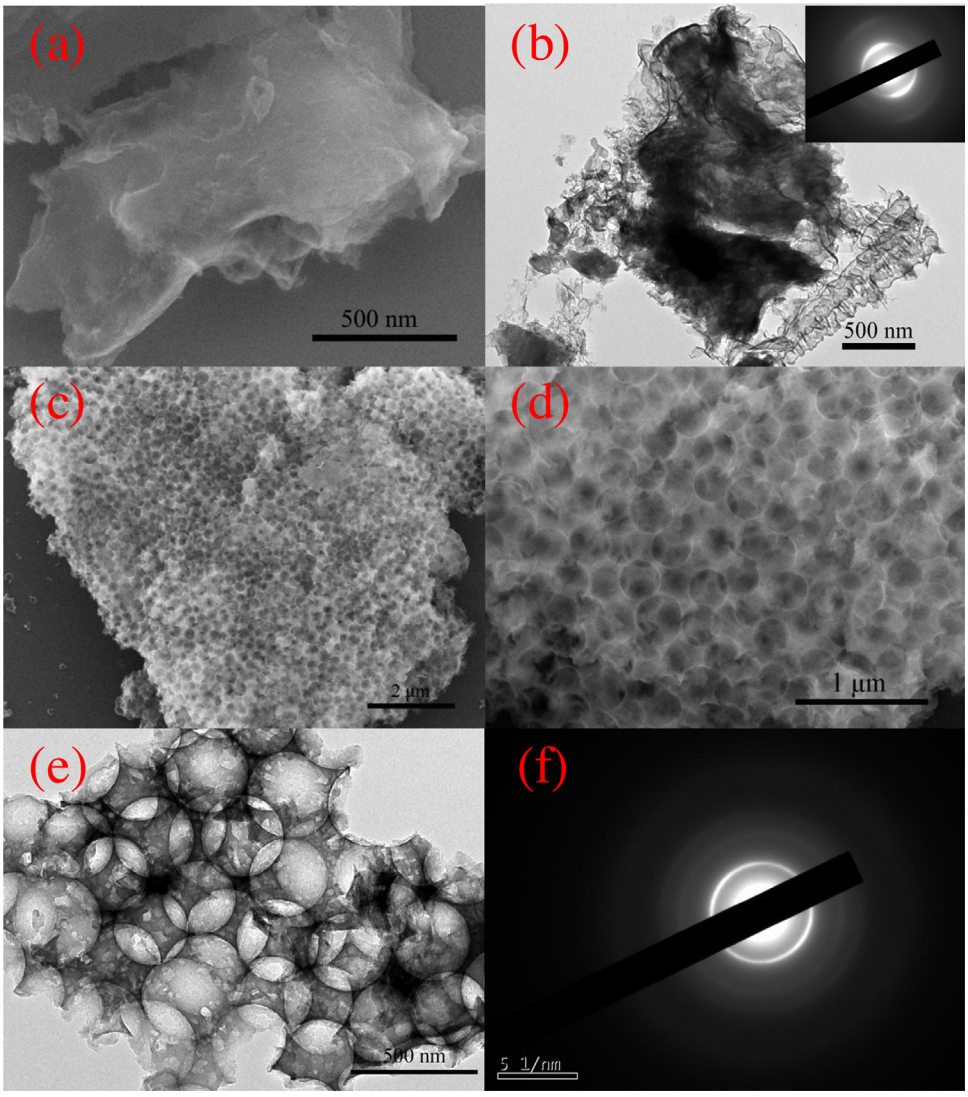

Fig. 3. SEM images of (a) pure g-C_3N_4 and (c, d) 3DOM g-C_3N_4; TEM images of (b) pure g-C_3N_4 and (e) 3DOM g-C_3N_4; SAED images of (b, inset) pure g-C_3N_4 and (f) 3DOM g-C_3N_4.

mesoporous shell. These presented pore structure could provide plenty of necessary space for the cyanamide liquid loading. With an increase of aging time, countless cyanamide molecules were filled into the interstices of 3D SiO_2 opal frame and the mesoporous shell to obtain 3D cyanamide/silica hybrids, which can be conveniently converted to 3D g-C_3N_4/silica composite via thermal condensation of cyanamide calcining at 550 °C. At last, the final 3DOM g-C_3N_4 can be produced after removing the 3D SiO_2 template by hydrofluoric acid.

Fig. S1 shows the SEM and TEM images of the solid SiO_2 core and the resulting mesoporous core-shell SiO_2 nanospheres. As shown in Fig. S1a–c, the solid SiO_2 cores present monodisperse nanospherical structure with an average diameter of around 210 nm. In Fig. S1d, it can be observed from the large area SEM image that numerous ordered and closely packed SiO_2 core-shell nanospheres were adhered to form the three-dimensional periodic array structure. Furthermore, both the SEM and TEM images (Fig. S1e–f) of the 3D SiO_2 template indicate the uniform silica sphere with an average diameter of around 310 nm, and which also clearly present a representative core-shell structure with a solid core of about 210 nm and a mesoporous shell of about 50 nm. Besides, the textural information of the SiO_2 core and 3D core-shell SiO_2 template (Fig. S2 and Table S1) shows that the average mesoporous size of the core-shell SiO_2 is centralized at 5.64 nm, which has a little increase in comparison with solid SiO_2 core, indicating that the mesoporous SiO_2 shell has been successfully covered on the outside surface of SiO_2 core, however, the slight reduction of pore volume and BET surface area of the core-shell SiO_2 may be due to the blocking of partial pore channels.

Fig. 2a shows the X-ray diffraction patterns of pure g-C_3N_4 and 3DOM g-C_3N_4. It was clear that both of the samples have similar XRD profiles, and the sharp peak at around 27.3° can be indexed to the (002) crystal plane of g-C_3N_4 due to the interlayer stacking of melon networks of g-C_3N_4, while a minor peak at around 13.0° can be attributed to the (100) crystal plane of g-C_3N_4 due to the repetitive in-plane tri-s-triazine units [20,21]. To be carefully compared, it could be observed that the above-mentioned two peaks presented gradually increasing intensity from nanoparticle to 3DOM structure, indicating that the construction of 3DOM microstructure is beneficial for the improvement of g-C_3N_4 crystalline degree. In comparison with the lamellar g-C_3N_4, the (002) reflection peak of 3DOM g-C_3N_4 sample showed a tiny shift from 27.2° to 27.4°, this phenomena may be caused by the increased internal compaction in the 3DOM structure [22]. Fig. 2b shows the FT-IR spectra of pure g-C_3N_4 and 3DOM g-C_3N_4. These profiles of samples present a similar trend and several obvious peaks can be

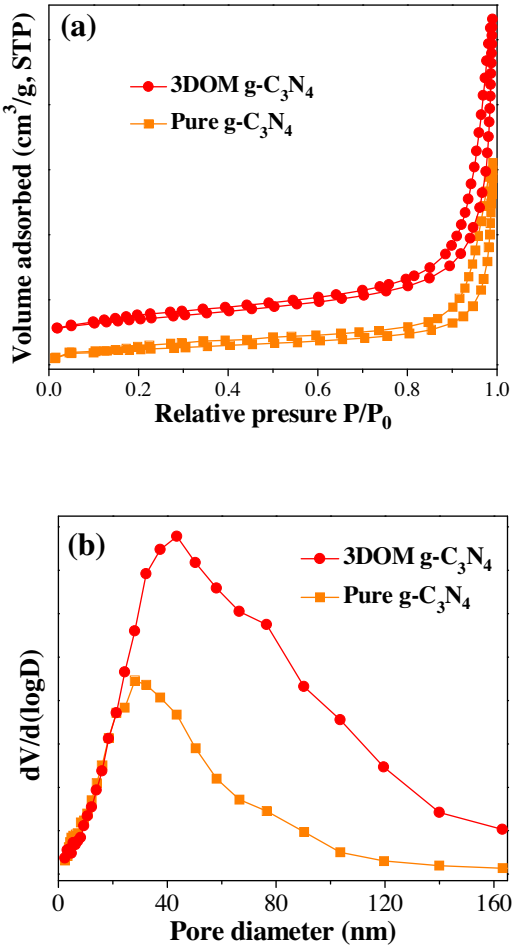

Fig. 4. Nitrogen adsorption-desorption isotherms (a) and pore-size distributions (b) of pure g-C_3N_4 and 3DOM g-C_3N_4.

easily observed: the bands centered at around 809 cm^{-1} and in the range of 1200–1700 cm^{-1} could be assigned to the bending modes of triazine ring motifs and the stretching modes of CN heterocycles [23,24], respectively. The bands at 3165 cm^{-1} and at 3682 cm^{-1} correspond to the N-H components (secondary and primary amines) [25] and the hydroxyl groups [26,27], respectively.

Fig. 3 shows the typical SEM and TEM images together with the SAED images of pure g-C_3N_4 and 3DOM g-C_3N_4. It can be seen from Fig. 3a–b that pure g-C_3N_4 presents a typical wrinkle two-dimensional lamellar structure composed with massive particles. Fig. 3c–e show the representative morphology of 3DOM g-C_3N_4. Both SEM and TEM images reveal that the 3DOM g-C_3N_4 photocatalyst presents a well-defined interconnected macroporous architecture with the average pore diameter of 280–340 nm. Interestingly, numerous nanopores with the size of 20–40 nm existed on the well-defined macroporous skeleton can be naturally observed from Fig. 3e, suggestive of the co-existence of mesopores and macropores in the 3DOM g-C_3N_4 sample. The selected area electron diffraction (SAED) image of pure g-C_3N_4 is shown in the inset of Fig. 3b. It can be clearly observed that pure g-C_3N_4 shows a relatively unclear bright electron diffraction ring, suggestive of an inferior crystallinity for this sample, however, the SAED pattern in Fig. 3f shows that the 3DOM g-C_3N_4 has the poly-crystalline nature and owns good crystallinity, which is in agreement with the XRD data.

Fig. 4 shows the nitrogen adsorption-desorption isotherms and pore-size distribution curves of pure g-C_3N_4 and 3DOM g-C_3N_4, respectively. It can be found (Fig. 4a) that both of the carbon nitride

Table 1
BET surface areas, average pore sizes and pore volumes of pure g-C_3N_4 and 3DOM g-C_3N_4.

Samples	S_{BET} ($m^2\ g^{-1}$)	Average pore size (nm)	Pore volume ($cm^3\ g^{-1}$)
Pure g-C_3N_4	9.74	21.28	0.0679
3DOM g-C_3N_4	24.63	34.84	0.1503

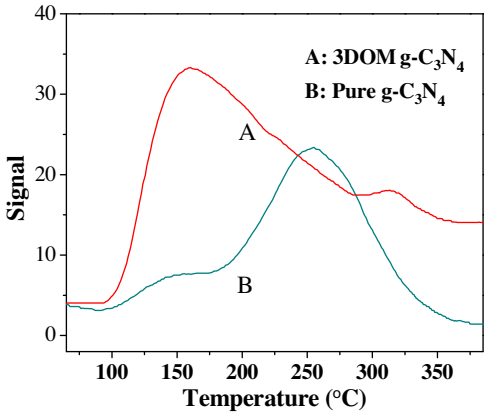

Fig. 5. CO_2-TPD profiles of pure g-C_3N_4 and 3DOM g-C_3N_4.

samples display a typical II isotherm with a type H3 hysteresis loop in the relative pressure (p/p_0) range of 0.4–1.0 according to the IUPAC classification, indicating that the presence of characteristic macropores in the two samples [9,11]. It should be mentioned that the pure g-C_3N_4 with the macroporous structure may be derived from the random interstitial holes formed by aggregating of massive g-C_3N_4 particles. As shown in Fig. 4b, the two samples present a broad pore-size distribution curve (3–140 nm), indicating that the pore size distribution extends from mesopore range to macropore range. This further confirms that the two samples possess a clear macroporous structure.

Table 1 summarizes the BET surface areas, average pore sizes and pore volumes of the two samples. It can be seen that the 3DOM g-C_3N_4 shows a larger average pore size (34.84 nm) than that of pure g-C_3N_4 (21.28 nm), which further proves that numerous mesopores co-exist in the 3DOM g-C_3N_4 sample, agreeing with the observations of SEM and TEM. Importantly, 3DOM g-C_3N_4 presents a much larger pore volume and a much higher surface area (0.1503 $cm^3\ g^{-1}$ and 24.63 $m^2\ g^{-1}$, respectively) than those of pure g-C_3N_4 (0.0679 $cm^3\ g^{-1}$ and 9.74 $m^2\ g^{-1}$, respectively), indicating that the construction of 3DOM architecture favors the significant enhancement of surface area, and thus benefiting the improvement of photocatalytic activity.

With abundant nitrogen species from tri-s-triazine units, g-C_3N_4 is considered to own numerous Lewis basic sites [28,29]. As the most important interfacial chemical reaction active sites, these basic sites in the carbon nitride system play a vital role in the adsorption and activation of reactant molecules. Therefore, CO_2-TPD tests were carried out to study the surface basicity of pure g-C_3N_4 and 3DOM g-C_3N_4. As shown in Fig. 5, two CO_2 desorption peaks can be observed in both TPD curves, suggesting the presence of at least two types of surface basic sites in the two samples [30,31]. Herein, according to the surface properties of g-C_3N_4, it is inferred that the peak centered at around 159 °C can be attributed to the desorption of CO_2 adsorbed on the residual NH_2 groups, and the second peak located at high temperature region (250–350 °C) is corresponding to the amino groups (—NH and/or =NH) on the surface edges [32]. It is interesting to note that the area of CO_2 desorption peak directly reflects the amount of basic sites existed in

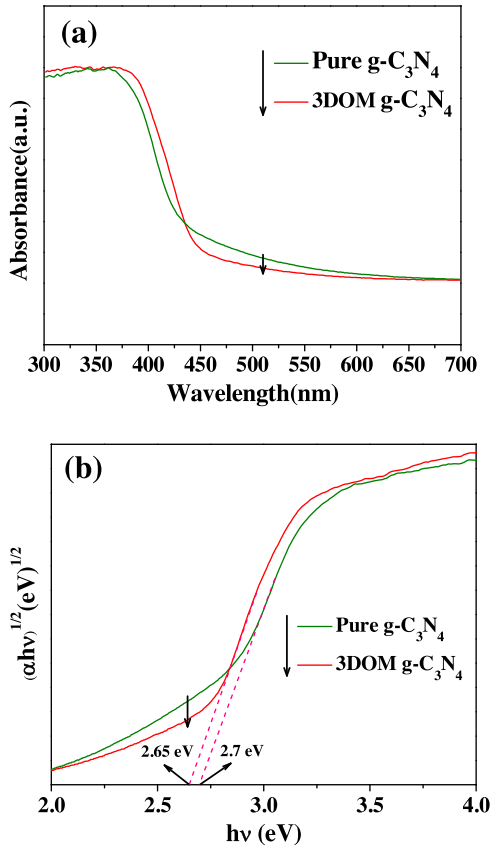

Fig. 6. (a) UV–vis diffuse reflectance spectra and (b) plots of $(\alpha h\nu)^{1/2}$ versus energy ($h\nu$) for pure g-C_3N_4 and 3DOM g-C_3N_4.

the samples. It can be seen that the peak area of 3DOM g-C_3N_4 is much larger than that of pure g-C_3N_4, indicating that 3DOM architecture is favorable for the construction of numerous surface basic sites, which can act as the chemical reaction active sites to response the high extent of capture of pollution molecules.

The UV–vis diffuse reflectance spectra of the as-prepared photocatalysts are displayed in Fig. 6a. It is apparent that pure g-C_3N_4 exhibits a routine light responsive ability in the visible light region with an absorption edge at up to 460 nm, which can be attributed to the intrinsic band gap of 2.7 eV for g-C_3N_4 [12,33]. Compared with pure g-C_3N_4, the absorption edge of 3DOM g-C_3N_4 sample has an obvious red shift that tempestuously extends to 468 nm, indicative of the narrower band gap. According to the UV–vis absorption spectra, we can see that the 3DOM features are great beneficial for the visible light harvest and the narrow optical band gap, this phenomenon can be ascribed to the multiple scattering and slow photon effects [3,8,34] as well as the periodic variation of the dielectric constant of 3DOM structure [35].

To calculate the band gap energy of the as-prepared samples, the plots of $(\alpha h\nu)^{1/2}$ versus energy ($h\nu$) for them have been explored on basis of the following formula:

$$\alpha h\nu = A(h\nu - E_g)^{n/2} \quad (2)$$

where α, h, ν, A, and E_g represent the absorption coefficient, Planck constant, light frequency, a constant and band gap energy, respectively, and the value of n for g-C_3N_4 is 4 because of its indirect transition band gap [36,37]. As shown in Fig. 6b, the E_g values for pure g-C_3N_4 and 3DOM g-C_3N_4 equal 2.7 eV and 2.65 eV, respectively. In addition, the valence band potential (E_{VB}) and the conduction band potential (E_{CB}) of these samples can be predicted by the following two equations:

$$E_{VB} = X - E_e + 0.5E_g \quad (3)$$

$$E_{CB} = E_{VB} - E_g \quad (4)$$

where X represents the electronegativity of the semiconductor and its value for g-C_3N_4 is 4.73 eV, E_e represents the energy of free electrons on the hydrogen scale with a fixed value of 4.5 eV [33,37]. Therefore, the E_{VB} values of pure g-C_3N_4 and 3DOM g-C_3N_4 can be estimated to be 1.58 eV and 1.56 eV, respectively, and the E_{CB} values of them are −1.12 eV and −1.09 eV accordingly.

To shed light on the influence of trapping, migration and recombination of the photoinduced charge carriers with the construction of 3DOM structure, the photoluminescence (PL) tests of the as-prepared samples were conducted under 340 nm excitation wavelength. As shown in Fig. 7a, all PL spectra of these samples exhibit similar trend. In the case of pure g-C_3N_4, an extremely high PL intensity peak can be observed, suggestive of a considerably high recombination probability of photogenerated charge carriers [38]. In comparison with pure g-C_3N_4, the PL emission intensity of 3DOM g-C_3N_4 dramatically descended, indicating that the successful construction of 3DOM architecture can greatly enhance the separation efficiency of photogenerated charge carriers of g-C_3N_4 under a longer wavelength visible-light irradiation.

The separation and transfer efficiency of the photoexcited charge carriers were probed by measuring the transient photocurrent response and the electrochemical impedance spectroscopy (EIS) of the as-prepared photocatalysts under visible light irradiation ($\lambda \geq 420$ nm). As shown in Fig. 7b, pure g-C_3N_4 exhibits a weak photocurrent response, suggestive of an inferior separation and transfer efficiency [39]. In contrast, the photocurrent response of 3DOM g-C_3N_4 has dramatically enhanced, implying that the formation of 3DOM architecture can obviously facilitate the separation and transfer of photogenerated charge carriers. This result is confirmed by the EIS measurement. As revealed in Fig. 7c, the diameter of the Nyquist circle of 3DOM g-C_3N_4 is much smaller than that of pure g-C_3N_4, demonstrating that the resistance of charge transfer at solid (3DOM g-C_3N_4)/liquid interface was obviously decreased, resulting in the effective improvement of the electronic conductivity in 3DOM g-C_3N_4.

To investigate the adsorption performances of g-C_3N_4 photocatalysts, the effects of contact time on the adsorption amount of RhB over different g-C_3N_4 samples were studied and the results are demonstrated in Fig. 8a. It is found that all the samples completely reached adsorption/desorption equilibrium within 5 min, indicating that the absorption process of RhB solution over the as-prepared photocatalysts is pretty fast, and we choose 40 min as the adsorption equilibrium time before the start of photocatalytic reaction is sufficient and rational. Besides, the 3DOM g-C_3N_4 shows the highest adsorption amount of RhB (1.57 mg g^{-1}), manifesting that the construction of 3DOM structure with numerous adsorption active sites is favorable for the mass transfer and capture, resulting in enhancement of the photoactivity.

The photodegradation of RhB solution (10 mg/L) over the obtained photocatalysts was tested under visible light irradiation ($\lambda \geq 420$ nm) to evaluate their application value of water treatment. Based on our previously reported work [21], the model pollution of RhB is quite stable and its photodegradation efficiency can be negligible in the absence of the photocatalysts under visible light irradiation ($\lambda \geq 420$ nm). As described in Fig. 8b, P25 TiO_2 possesses a modest visible-light-driven activity in the degradation of RhB (approximately 41% within 40 min irradiation), which can be ascribed to the photosensitization effect of RhB dye [19]. Moreover, the pure g-C_3N_4 sample exhibits the lowest photodegradation efficiency with an RhB conversion of 19% under the same reac-

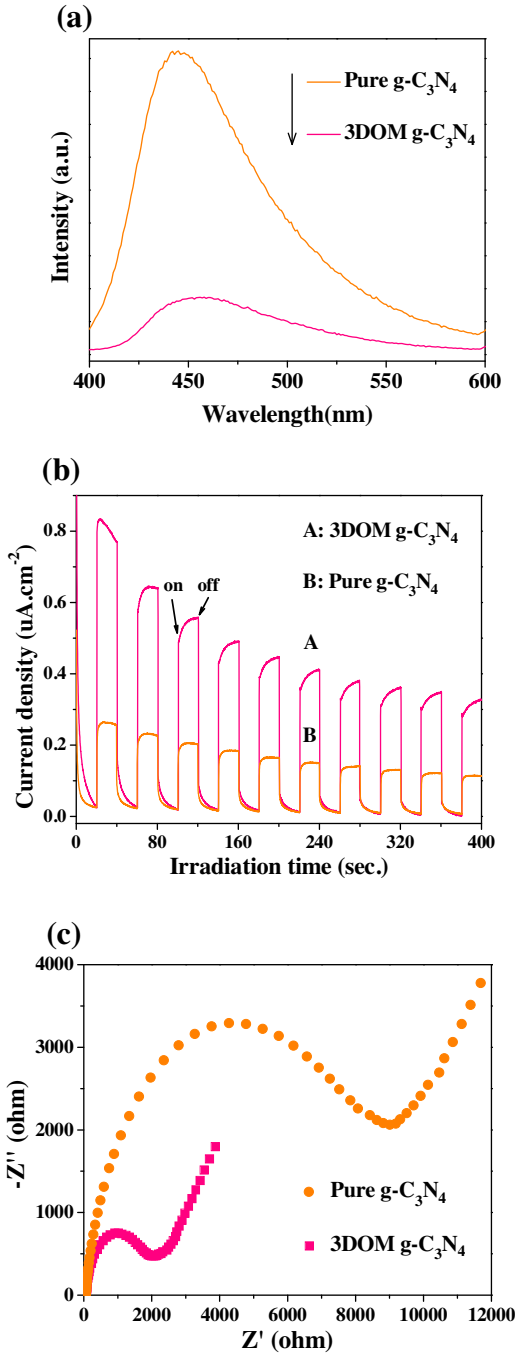

Fig. 7. (a) PL spectra of pure g-C_3N_4 and 3DOM g-C_3N_4 under 340 nm excitation wavelength; (b)Transient photocurrent responses and (c) EIS Nyquist plots of pure g-C_3N_4 and 3DOM g-C_3N_4 under visible light irradiation ($\lambda \geq 420$ nm).

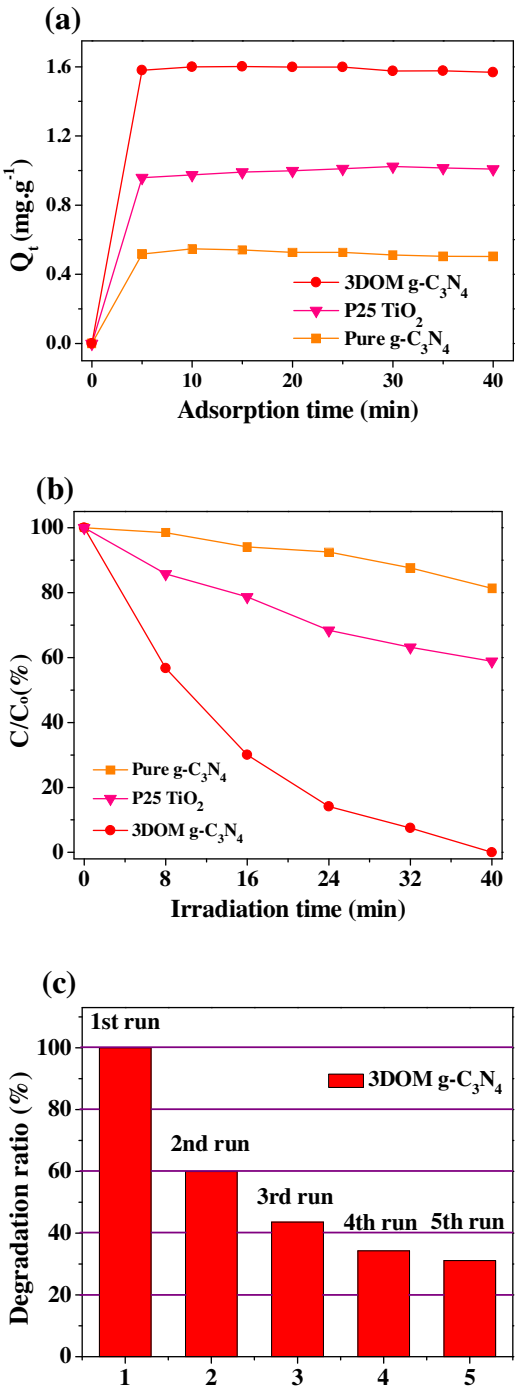

Fig. 8. (a) Adsorption equilibrium plots of RhB solution (10 mg/L) on pure g-C_3N_4, P25 TiO_2 and 3DOM g-C_3N_4; (b) Photodegradation efficiency plots of RhB solution (10 mg/L) over pure g-C_3N_4, P25 TiO_2 and 3DOM g-C_3N_4 under visible light irradiation ($\lambda \geq 420$ nm); (c) Cycling runs of 3DOM g-C_3N_4 for the photodegradation of RhB solution (10 mg/L) over under visible light irradiation ($\lambda \geq 420$ nm).

tion condition, which attributes to the lamellar g-C_3N_4 with the high recombination efficiency of the photogenerated electron-hole pairs. Incredibly, the 3DOM g-C_3N_4 sample displays dramatically enhanced photodegradation efficiency with an RhB conversion of 100% within 40 min photoreaction, which is approximately 5.3 times higher than that of pure g-C_3N_4, confirming again that the fabrication of 3DOM architecture is extremely beneficial for the enhancement of photocatalytic activity of 3DOM g-C_3N_4.

To investigate the performance of stability and recyclability for the 3DOM g-C_3N_4 sample, the recycled tests of photodegradation RhB (10 mg/L) over 3DOM g-C_3N_4 were performed within 40 min visible-light irradiation. As illustrated in Fig. 8c, 3DOM g-C_3N_4 exhibits an extremely excellent photocatalytic activity for degrading RhB and completely mineralizes RhB within 40 min photoreaction in the initial cycle test, unfortunately, starting from the second cycle test, the degradation ratio of RhB over 3DOM g-C_3N_4 has continuously declined (from approximately 60% to 43.6%, then to 34.3%), and the photodegradation efficiency of RhB was only closed to be 32% in the fifth cycle test within 40 min photoreaction, which is still higher than that of pure g-C_3N_4. Fig. S3 shows the TEM images of 3DOM g-C_3N_4 after the 5th run recycled test. It can

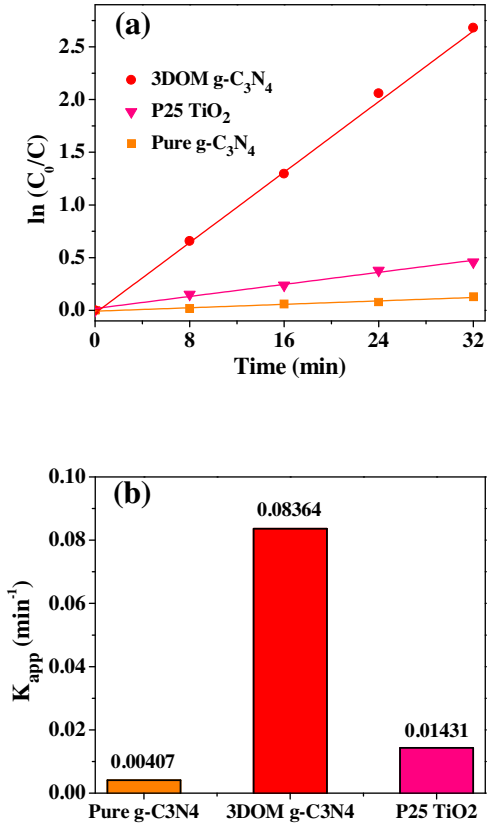

Fig. 9. (a) Kinetic curves for the degradation of RhB over pure g-C_3N_4, P25 TiO_2 and 3DOM g-C_3N_4; (b) Values of apparent rate constants for the degradation of RhB over pure g-C_3N_4, P25 TiO_2 and 3DOM g-C_3N_4.

be seen that the basic 3DOM framework of the as-obtained g-C_3N_4 remains relatively intact, indicating that 3DOM g-C_3N_4 owns better mechanical strength and stability, which may have an excellent application potential in water treatment.

To intuitively comprehend the aforementioned photodegradation performance, the photodecomposition kinetics over different samples was quantitatively probed. Based on Langmuir-Hinshelwood model, the kinetic behaviors of the RhB degradation can be obeyed the following equation [40,41]:

$$\ln(C_0/C) = k_{app}t \quad (5)$$

where C_0 and C represent the initial and instantaneous (at reaction time t) concentration of RhB, respectively, and k_{app} represents the apparent reaction rate constant. As depicted in Fig. 9a, an apparent linear relationship between the dependent variable of $\ln(C_0/C)$ and the independent variable of t can be observed, suggesting that the photodecomposition kinetics is consistent with the pseudo-first-order mode. The values of apparent pseudo-first-order rate constant (k_{app}) are equal to 0.00407, 0.01431 and 0.08364 min^{-1} for pure g-C_3N_4, P25 TiO_2 and 3DOM g-C_3N_4, respectively (Fig. 9b). It is noted that the sample of 3DOM g-C_3N_4 exhibits the highest k_{app} value of 0.08364 min^{-1}, which is approximately 5.8 and 20.5 times higher than that of P25 TiO_2 and pure g-C_3N_4, respectively.

4. Discussions

On basis of the above mentioned demonstrations, the as-prepared 3DOM g-C_3N_4 possesses outstanding visible-light-driven photodegradation performance in comparison with pure g-C_3N_4, implying a potential application in water treatment.

In order to discuss the origin of the superior photoactivity over 3DOM g-C_3N_4 photocatalyst, it seems to be advisable to analyze the advanced structure because the 3DOM architecture shows somewhat special structure sensitive properties for the light trapping and mass transfer of the reactant, which make the material present a high intrinsic activity. In this work, the structure sensitive property for the 3DOM g-C_3N_4 sample can be demonstrated by the following three aspects. Firstly, as mentioned in the analysis of XRD and FT-IR, both 3DOM g-C_3N_4 and pure g-C_3N_4 samples show the similar peak positions and the same element components, however, combined with the SAED characterization results, the novel 3DOM structure sample possesses a much stronger diffraction intensity, indicative of a high crystalline degree for the 3DOM g-C_3N_4, which favors charge transfer and conduction from the crystal bulk to the interface between solid and reactant molecules. Secondly, through observations of SEM and TEM images, it is found that a large number of mesopores have been introduced into the 3DOM skeleton, and these formed mesopores together with the 3D macroporous structure can offer a larger active surface area and higher porosity (Table 1), which is beneficial to increase the number of interfacial reaction active sites (adsorption measurement and TPD tests), and thus contributes to the adsorption, photoreaction and desorption of the reactant molecules within the degradation of organic pollution. Lastly, the 3DOM architecture can provide numerous optical absorption active sites as well, which is very sensitive to the photon trapping and energy band gap narrowing. As shown in Fig. 6, owing to the inimitable multiple scattering and slow photon effects of 3DOM structure, the path length of light in the 3DOM g-C_3N_4 system would be prolonged and thus leads to a longer wavelength range of visible light harvesting. Moreover, the 3D interconnected macroporous networks consisted of periodic spherical voids possess the property of periodic variation of the dielectric constant [35], leading to the slight reduction of the energy band gap of g-C_3N_4. Therefore, the longer wavelength of visible light could be absorbed by the 3DOM g-C_3N_4, and excite the material to produce a large number of electron-hole pairs, the photogenerated charges subsequently would be easily transfer from the bulk to the surface, resulting in the great improvement of the charge separation efficiency (see the results of PL and photocurrent measurements). According to the aforementioned discussions, it is clear that the superior photocatalytic activity of the as-obtained 3DOM g-C_3N_4 arises from the synergistic effect of the high crystallinity, stronger photon trapping and absorption as well as the larger active surface area and higher porosity.

Furthermore, the quenching experiments of 3DOM g-C_3N_4 were carried out relying on different scavengers to ascertain the main active species in the photoreaction process. In this work, benzoquinone (BQ), disodium ethylenediaminetetraacetate dehydrate (EDTA-2Na) and 2-propanol (IPA) were employed as the quenchers of $^{\bullet}O_2^-$, h^+ and $^{\bullet}OH$, respectively [33,40]. As shown in Fig. 10, the 3DOM g-C_3N_4 sample shows an extremely excellent photodegradation efficiency of RhB (up to 100%) in the absence of the scavengers within 40 min irradiation. Along with the participation of IPA in the photoreaction, the decolorization of RhB was slightly hindered and still could be up to 95.8%, signifying that $^{\bullet}OH$ was not the key active species for oxidating RhB in the photodegradation progress. In contrast, when the scavengers of EDTA-2Na and BQ were respectively added into the photoreaction system, a dramatic decline related to the photodegradation efficiency of RhB could be observed (reducing to 60.5% and 29.6%, respectively), indicating that the h^+ and $^{\bullet}O_2^-$ play a vital roles in the photoreaction, both of them are the primary reactive species to respond for the decomposition of organic dye with using 3DOM g-C_3N_4 photocatalyst.

Based on the aforementioned results and discussion, a possible visible-light-driven photocatalytic reaction mechanism of RhB degradation in the presence of 3DOM g-C_3N_4 has been proposed.

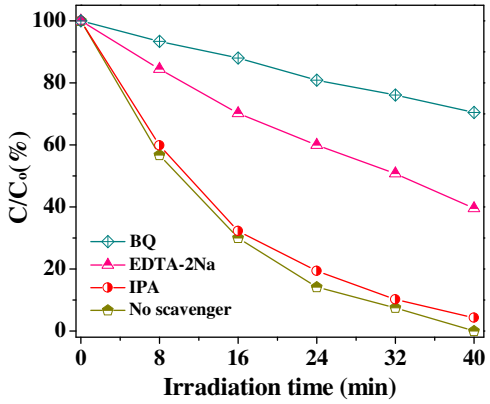

Fig. 10. Effects of different scavengers on the photodegradation efficiency of RhB solution (10 mg/L) over 3DOM g-C_3N_4.

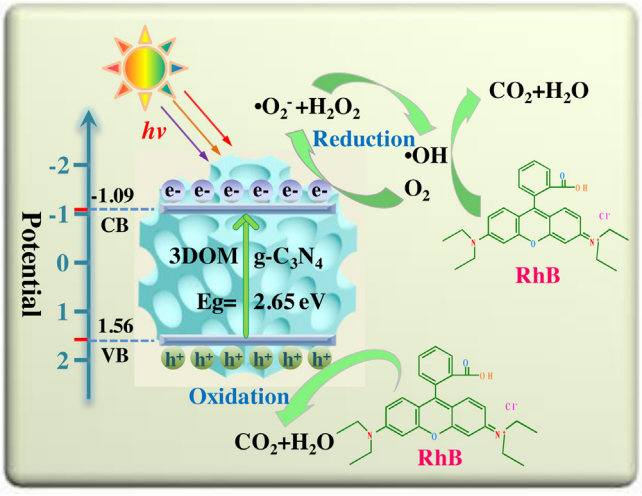

Fig. 11. Schematic illustration of photocatalytic reaction mechanism of RhB degradation in the presence of 3DOM g-C_3N_4 under visible light irradiation ($\lambda \geq 420$ nm).

As illustrated in Fig. 11, the optical absorption active sites on 3DOM g-C_3N_4 could absorb a great deal of visible light to yield photogenerated electron-hole pairs. The photoexcited electrons were then rapidly transfered to the conduction band (CB) of 3DOM g-C_3N_4, leaving behind the photoexcited holes on the valence band (VB) of the material. Because the E_{CB} value of 3DOM g-C_3N_4 (−1.09 eV) is more negative than that of $O_2/{}^{\bullet}O_2^-$ (−0.33 eV vs. NHE) [42], therefore, the photogenerated electrons in the CB of 3DOM g-C_3N_4 could easily react with oxygen molecules absorbed on the interfacial reaction active sites or dissolved in aqueous solution to produce the superoxide radical (${}^{\bullet}O_2^-$) and the hydrogen peroxide (H_2O_2) [19,43], and both of the species can further react each other to create the hydroxyl radical (•OH). The active species of ${}^{\bullet}O_2^-$ and •OH can continuously attack the RhB dye until it is completely mineralized into CO_2 and H_2O. On the other hand, the E_{VB} value of 3DOM g-C_3N_4 (+1.56 eV) is more negative than those of $^{\bullet}OH/OH^-$ (+1.99 eV vs. NHE) and $^{\bullet}OH/H_2O$ (+2.27 eV vs. NHE), thus the residual photoexcited holes on the VB of 3DOM g-C_3N_4 cannot oxidize the adsorbed H_2O molecules or hydroxyl (OH^-) to generate the hydroxyl radical (•OH) [42], suggesting that the •OH is not the primary reactive species in the photodegradation process, which is consistent with the results of the quenching experiments. However, the holes accumulated in the 3DOM g-C_3N_4 can directly oxidize RhB molecules into the end products. Therefore, the cooperative work of ${}^{\bullet}O_2^-$ and h^+ ultimately result in the significant enhancement of photodegradation activity for the 3DOM g-C_3N_4 photocatalyst.

5. Conclusions

The novel 3DOM g-C_3N_4 was successfully constructed by a simply thermal condensation-assisted colloidal crystal template method. The results show that 3DOM g-C_3N_4 displays a dramatically enhanced photocatalytic activity with an RhB photodegradation efficiency of 100% within 40 min visible-light illumination, which was approximately 5.3 times higher than that of pure g-C_3N_4. Besides, it is found that the holes and superoxide radical are the primary reactive species in the photodegradation process in the presence of 3DOM g-C_3N_4 photocatalyst. The optical absorption active sites and the interfacial reaction active sites over the three dimensionally ordered macroporous structure contribute to the light trapping, the charge carriers separation and the mass transfer, and the synergetic action of all the above factors is responsible for the significant enhancement of photocatalytic performance. This work has demonstrated the unique advantages of 3DOM architecture, which can provide new insight for the design of high-performance photocatalytic materials.

Acknowledgements

This work was financially supported by the National Natural Science Foundation of China (Grant No. 21303130), the Natural Science Basic Research Plan in Shaanxi Province of China (Grant No. 2014JQ2066) and the Fundamental Research Funds for the Central Universities. Thanks for the technical support from International Center for Dielectric Research (ICDR), Xi'an Jiaotong University, Xi'an, China; the authors also appreciate Ms. Dai and Mr. Ma for their help in using SEM, EDX and TEM, respectively.

Appendix A. Supplementary data

Supplementary data associated with this article can be found, in the online version, at http://dx.doi.org/10.1016/j.apcatb.2016.05.069.

References

[1] J. Xie, X.H. Yao, Q.M. Cheng, I.P. Madden, P. Dornath, C.C. Chang, W. Fan, D.W. Wang, Angew. Chem. Int. Ed. 54 (2015) 4299–4303.
[2] H. Arandiyan, H.X. Dai, K.M. Ji, H.Y. Sun, J.H. Li, ACS Catal. 5 (2015) 1781–1793.
[3] Y.C. Wei, J.Q. Jiao, Z. Zhao, W.J. Zhong, J.M. Li, J. Liu, G.Y. Jiang, A.J. Duan, J. Mater. Chem. A 3 (2015) 11074–11085.
[4] A. Stein, B.E. Wilson, S.G. Rudisill, Chem. Soc. Rev. 42 (2013) 2763–2803.
[5] M. Sadakane, K. Sasaki, H. Nakamura, T. Yamamoto, W. Ninomiya, W. Ueda, Langmuir 28 (2012) 17766–17770.
[6] Y.J. Jiang, Y.P. Wang, H. Wang, L.Y. Zhou, J. Gao, Y.F. Zhang, X. Zhang, X.M. Wang, J. Li, New J. Chem. 39 (2015) 978–984.
[7] M.J. Deng, C.Z. Song, P.J. Ho, C.C. Wang, J.M. Chen, K.T. Lu, Phys. Chem. Chem. Phys. 15 (2013) 7479–7483.
[8] T. Wang, X.Q. Yan, S.S. Zhao, B. Lin, C. Xue, G.D. Yang, S.J. Ding, B.L. Yang, C.S. Ma, G. Yang, G.R. Yang, J. Mater. Chem. A 2 (2014) 15611–15619.
[9] K.M. Ji, J.G. Deng, H.J. Zang, J.H. Han, H. Arandiyan, H.X. Dai, Appl. Catal. B: Environ. 165 (2015) 285–295.
[10] Y.J. Zhang, J.G. Deng, H. Zhang, Y.X. Liu, H.X. Dai, Catal. Today 245 (2015) 28–36.
[11] S.H. Xie, J.G. Deng, S.M. Zang, H.G. Yang, G.S. Guo, H. Arandiyan, H.X. Dai, J. Catal. 322 (2015) 38–48.
[12] X.C. Wang, K. Maeda, A. Thomas, K. Takanabe, G. Xin, J.M. Carlsson, K. Domen, M. Antonietti, Nat. Mater. 8 (2009) 76–80.
[13] Y. Wang, X.C. Wang, M. Antonietti, Angew. Chem. Int. Ed. 51 (2012) 68–89.
[14] E.G. Gillan, Chem. Mater. 12 (2000) 3906–3912.
[15] Y.J. Zhang, T. Mori, J.H. Ye, M. Antonietti, J. Am. Chem. Soc. 132 (2010) 6294–6295.
[16] S. Kumar, T. Surendar, A. Baruahb, V. Shanker, J. Mater. Chem. A 1 (2013) 5333–5340.
[17] X.C. Wang, K. Maeda, X.F. Chen, K. Takanabe, K. Domen, Y.D. Hou, X.Z. Fu, M. Antonietti, J. Am. Chem. Soc. 131 (2009) 1680–1681.
[18] J. Liang, Y. Zheng, J. Chen, J. Liu, D.H. Jurcakova, M. Jaroniec, S.Z. Qiao, Angew. Chem. Int. Ed. 51 (2012) 3892–3896.
[19] C. Xue, T. Wang, G.D. Yang, B.L. Yang, S.J. Ding, J. Mater. Chem. A 2 (2014) 7674–7679.

[20] T.Y. Ma, S. Dai, M. Jaroniec, S.Z. Qiao, Angew. Chem. Int. Ed. 53 (2014) 7281–7285.
[21] B. Lin, C. Xue, X.Q. Yan, G.D. Yang, G. Yang, B.L. Yang, Appl. Surf. Sci. 357 (2015) 346–355.
[22] Y.J. Zhou, L.X. Zhang, J.J. Liu, X.Q. Fan, B.Z. Wang, M. Wang, W.C. Ren, J. Wang, M.L. Li, J.L. Shi, J. Mater. Chem. A 3 (2015) 3862–3867.
[23] L. Shi, L. Liang, J. Ma, F.X. Wang, J.M. Sun, Dalton Trans. 43 (2014) 7236–7244.
[24] H.J. Li, B.W. Sun, L. Sui, D.J. Qian, M. Chen, Phys. Chem. Chem. Phys. 17 (2015) 3309–3315.
[25] T. Jayaraman, S.A. Raja, A. Priya, M. Jagannathan, M. Ashokkumar, New J. Chem. 39 (2015) 1367–1374.
[26] F.R. Meng, J.L. Yu, A. Tahmasebi, Y.N. Han, H. Zhao, J. Lucas, T. Wall, Energy Fuels 28 (2014) 275–284.
[27] B. Szczepanik, P. Słomkiewicz, M. Garnuszek, K. Czech, D. Banaś, A.K. Kukuś, I. Stabrawa, J. Mol. Struct. 1084 (2015) 16–22.
[28] D.H. Lan, H.T. Wang, L. Chen, C.T. Au, S.F. Yin, Carbon 100 (2016) 81–89.
[29] Q. Li, J.P. Yang, D. Feng, Z.X. Wu, Q.L. Wu, S.S. Park, C.S. Ha, D.Y. Zhao, Nano Res. 3 (2010) 632–642.
[30] J. Xu, Y. Wang, J.K. Shang, Q. Jiang, Y.X. Li, Catal. Sci. Technol. (2016).
[31] Q. Yang, W.Y. Wang, Y.X. Zhao, J.J. Zhu, Y.J. Zhu, L.H. Wang, RSC Adv. 5 (2015) 54978–54984.
[32] S.N. Talapaneni, S. Anandan, G.P. Mane, C. Anand, D.S. Dhawale, S. Varghese, A. Mano, T. Mori, A. Vinu, J. Mater. Chem. 22 (2012) 9831–9840.
[33] S.F. Chen, Y.F. Hu, S.G. Meng, X.L. Fu, Appl. Catal. B: Environ. 150–151 (2014) 564–573.
[34] J.Q. Jiao, Y.C. Wei, Z. Zhao, J. Liu, J.M. Li, A.J. Duan, G.Y. Jiang, Ind. Eng. Chem. Res. 53 (2014) 17345–17354.
[35] L. Li, X.D. Huang, T.Y. Hu, J.X. Wang, W.Z. Zhang, J.Q. Zhang, New J. Chem. 38 (2014) 5293–5302.
[36] N. Tian, H.W. Huang, Y.X. Guo, Y. He, Y.H. Zhang, Appl. Surf. Sci. 322 (2014) 249–254.
[37] J.F. Zhang, Y.F. Hu, X.L. Jiang, S.F. Chen, S.G. Meng, X.L. Fu, J. Hazard. Mater. 280 (2014) 713–722.
[38] H. Katsumata, T. Sakai, T. Suzuki, S. Kaneco, Ind. Eng. Chem. Res. 53 (2014) 8018–8025.
[39] C.Y. Liu, H.W. Huang, X. Du, T.R. Zhang, N. Tian, Y.X. Guo, Y.H. Zhang, J. Phys. Chem. C 119 (2015) 17156–17165.
[40] K. Li, S.M. Gao, Q.Y. Wang, H. Xu, Z.Y. Wang, B.B. Huang, Y. Dai, J. Lu, ACS Appl. Mater. Interfaces 7 (2015) 9023–9030.
[41] N. Tian, H.W. Huang, Y. He, Y.X. Guo, T.R. Zhang, Y.H. Zhang, Dalton Trans. 44 (2015) 4297–4307.
[42] W.J. Wang, J.C. Yu, D.H. Xia, P.K. Wong, Y.C. Li, Environ. Sci. Technol. 47 (2013) 8724–8732.
[43] S.N. Xiao, W. Zhu, P.J. Liu, F.F. Liu, W.R. Dai, D.Q. Zhang, W. Chen, H.X. Li, Nanoscale 8 (2016) 2899–2907.